Journal of Nuclear Medicine, published on June 14, 2018 as doi:10.2967/jnumed.118.208827

Performance evaluation of G8, a high sensitivity benchtop preclinical PET/CT tomograph

Zheng Gu[1, 2], Richard Taschereau[1], Nam T Vu[2], David L Prout[1], Robert W Silverman[1], Jason Lee[1, 3], and Arion F Chatziioannou[1, 2, 3]

[1] Crump Institute for Molecular Imaging, David Geffen School of Medicine, University of California, Los Angeles, Los Angeles, CA, USA

[2] Sofie Biosciences, Culver City, California, USA

[3] Jonsson Comprehensive Cancer Center, University of California, Los Angeles, Los Angeles, CA, USA

The first author and the author responsible for correspondence:

Name: Zheng Gu

Address: 570 Westwood Plaza, Crump Institute for Molecular Imaging, Los Angeles, CA 90095

Phone: 310-825-5559

E-mail: zhgu@mednet.ucla.edu

Fax number: 310-206-8975

The first author is not currently in training.

This work was supported by the UCLA Foundation from a donation made by Ralph and Marjorie Crump for the UCLA Crump Institute for Molecular Imaging and in part by the National Cancer Institute P30 CA016042 Cancer Center Support Grant.

Short Running Title: Performance evaluation of G8

ABSTRACT

G8 is a bench top integrated PET/CT scanner dedicated to high sensitivity and high resolution imaging of mice. This work characterizes its National Electrical Manufacturers Association (NEMA) NU4-2008 performance where applicable and also provides an assessment of the basic imaging performance of the CT subsystem.

Methods: The PET subsystem in G8 consists of four flat-panel type detectors arranged in a box like geometry. Each panel consists of two modules of a 26 × 26 pixelated bismuth germanate (BGO) scintillator array with individual crystals measuring 1.75 × 1.75 × 7.2 mm. The crystal arrays are coupled to multichannel photomultiplier tubes via a tapered, pixelated glass lightguide. A cone-beam CT consisting of a micro focus X-ray source and a Complementary Metal Oxide Semiconductor (CMOS) detector provides anatomical information. Sensitivity, spatial resolution, energy resolution, scatter fraction, count-rate performance and the capability of phantom and mouse imaging were evaluated for the PET subsystem. Noise, dose level, contrast and resolution were evaluated for the CT subsystem.

Results: With an energy window of 350–650 keV, the peak sensitivity was measured to be 9.0% near the center of the field of view (CFOV). The crystal energy resolution ranged from 15.0% to 69.6% full width at half maximum (FWHM), with a mean of 19.3 ± 3.7%. The average detector intrinsic spatial resolution was 1.30 mm and 1.38 mm FWHM in the transverse and axial directions. The maximum likelihood expectation maximization (ML-EM) reconstructed image of a point source in air, averaged 0.81 ± 0.11 mm FWHM. The peak noise equivalent count rate (NECR) for the mouse-sized phantom was 44 kcps for a total activity of 2.9 MBq (78 μCi) and the scatter fraction was 11%. For the CT subsystem, the value of the modulation transfer function (MTF) at 10% was 2.05 cycles/mm.

Conclusion: The overall performance demonstrates that the G8 can produce high quality images for molecular imaging based biomedical research.

Key Words: small animal imaging; PET/CT, performance evaluation; instrumentation; molecular imaging

INTRODUCTION

Positron emission tomography (PET) is a widely used imaging modality for non-invasive, *in vivo* studies of biological processes and has found wide application in pharmacology, genetics, pathology and oncology (*1,2*). The demand for *in vivo* experiments with animal models of disease in translational research has been a driving force behind the advances of dedicated small animal PET instruments (*3,4*).

In molecular imaging applications, anatomical reference is commonly required to help localize the molecular signal and assist quantification of tracer concentration (*5,6*). Computed tomography (CT) is a modality that can provide fully tomographic anatomical information for better molecular signal localization (*7*). Volumetric CT data also facilitates tracer quantification by guiding corrections for attenuation (*8*), scattering of gammas in the object (*9*), and partial volume effect (*10*). Besides, CT leads to an accurate organ registration and image analysis when used with the mouse atlas registration algorithm developed in our institute (*11*).

G8, is an integrated PET/CT system, implemented by Sofie Biosciences (Culver City, CA). It incorporates a cone-beam CT, and digital data acquisition electronics (PicoDigitizer, Nutaq, Quebec). Compared to the previous G4 system (*12,13*), each panel detector employs two extra rows of crystals at the transverse edges of the field of view (FOV), reducing the gap between detectors. Instead of a 1 mm clear glass in G4, a tapered, pixelated lightguide, is used in G8 to couple each crystal array to a single photomultiplier tube (PMT), improving scintillation light collection and its uniformity.

This work aims to characterize the overall performance of the G8 PET/CT system. Studies including sensitivity, spatial resolution, energy resolution, scatter fraction, count-rate performance and image quality were performed for the PET subsystem following the National Electrical Manufacturers Association (NEMA) NU 4-2008 standards (*14*) where possible. The noise, dose level, contrast and spatial resolution were evaluated for the CT subsystem. *In vivo* rodent studies using radiolabeled tracers were acquired to demonstrate the capability of the G8 for high sensitivity, high resolution molecular imaging. Representative

animal images are shown to emphasize the complementary nature of the molecular and anatomical information provided by this integrated PET/CT imaging platform.

MATERIALS AND METHODS

System Description

The G8 employs four opposing panel detectors placed at a face to face spacing of 5 cm, arranged in a compact, box like geometry. The effective area of each panel is 47.44 × 94.95 mm, large enough to cover the whole body of laboratory mice (18-40g). Each panel consists of two modules, and each module is comprised of a 26 × 26 pixelated bismuth germanate (BGO) scintillator array with individual crystals measuring 1.75 × 1.75 × 7.2 mm (±0.05mm) and a pitch of 1.83 mm (Proteus, Chagrin Falls, OH). The four long sides of each individual crystal and the entrance surface of the scintillator array were bonded with specular optical reflector (3M, St Paul, MN). A tapered, pixelated glass lightguide was used to couple the crystal array to the photosensitive area of a H8500 multianode photomultiplier tube (MAPMT; Hamamatsu Photonics, Bridgewater, NJ). The scintillator array, lightguide and MAPMT were permanently bonded with epoxy.

The front end read-out electronics of each detector are integrated in a printed circuit board directly connected to the PMT. A charge-division readout circuit is used to convert the 64 anode outputs from each MAPMT into energy and two position signals (X and Y), while the timing signal is obtained directly from the 12th dynode on the PMT. The signals from all eight detector modules (four signals per module) are digitized by 32 free running 125 MHz ADCs, at 14 bits per sample (PicoDigitizer, Nutaq, Quebec). These digital samples are then processed in a Xilinx Virtex-6 field programmable gate array (FPGA, Xilinx, San Jose, CA) in real time for event triggering, validation (*15*) and coincidence sorting. Energy discrimination is performed offline in software, during event histogramming. A delayed timing window method is implemented in the FPGA to estimate random coincidence event rates (*16*).

All measurements in this work were post processed with an energy window of 350–650 keV (*17*). The only exception to this is the sensitivity measurement, for which the lower energy threshold was varied

between 150 and 350 keV to show the influence of energy window on sensitivity. The coincidence timing window was set to 20 nsec. The acquired list-mode data were histogrammed into projection files with delayed events subtracted to correct for random coincidences. Component-based normalization (*18*) was applied to compensate for the differences in individual detector efficiencies, estimated from measurements of a cylindrical source filled with ^{18}F. The acceptance angles were not restricted by the system hardware, and all geometrically possible lines of response were acquired. For image reconstruction, the line of response with the largest acceptance angle crossing the field of view was 76 degrees in the transverse and 59 degrees in the axial direction. Fully 3D tomographic images were reconstructed by a maximum likelihood and expectation maximization (ML-EM) algorithm with incorporation of a system model based on a parameterized detector response (*19*). The system response matrix used in the MLEM reconstruction corresponds to symmetrical cubic voxels with a side equal to 1/4th of the pitch of the crystals in the detector, and the cubic voxel size is 0.46 x 0.46 x 0.46 mm^3. A total of 60 full iterations (no subsets) were used for image reconstruction with no regularization, and no post-reconstruction smoothing was applied. The rectangular system geometry precludes the use of conventional linear image reconstruction algorithms.

A cone-beam CT consisting of a micro focus X-ray (50kV Magnum, Moxtek, Orem, UT) and a Complementary Metal Oxide Semiconductor (CMOS) detector (Dexela 1512, PerkinElmer, Santa Clara, CA) is implemented to provide anatomical information, assisting PET signal localization and quantification. The CT runs in continuous rotation mode and acquires 720 projections over one full 360 degree rotation in about one minute. The x-ray source operates at 50 kVp with a maximum anode current of 200 μA. Images were reconstructed with a Feldkamp filtered back-projection algorithm (ramp filter) and a voxel size of 0.2 mm (*20*). The reconstructed field of view of the CT is 5 × 5 × 10 cm. The CT and PET subsystems in the G8 are mounted on a common gantry with a shared life supporting chamber (*21*). The inherent co-registration of the functional PET images and anatomical CT images is achieved with a calibration step in a common spatial frame (*22*). A schematic of the G8 PET/CT scanner is shown in Figure 1, while the characteristics of the G4 and the G8 systems are summarized in Table 1.

Energy Resolution

A 0.22 MBq ^{68}Ge cylindrical source (Eckert & Ziegler Isotope Products, Valencia, CA) with a diameter of 37 mm and 100 mm length was placed at the center of the field of view (CFOV) of the PET subsystem to acquire a two-dimensional flood irradiation for each detector module. A semi-automated program defined the crystal look-up tables (LUT) that classify regions in the flood image into the proper crystal of the scintillator array. Energy spectra of individual crystals were extracted based on the LUTs and a Gaussian function was fitted to the photopeak of each energy spectra. Energy resolution was measured for every crystal in the scanner as the full width at half-maximum (FWHM) of the Gaussian function divided by the energy corresponding to the center of the photopeak, expressed as a percentage resolution.

Spatial Resolution

A 0.34 MBq ^{22}Na point source with a nominal size of 0.3 mm, embedded in a 1cm^3 piece of acrylic was used (NEMA NU4 compliant, Eckert & Ziegler Isotope Products, Valencia, CA). Measurements were not corrected for the physical source dimensions, positron range, or non-collinearity of positron annihilation gammas.

Intrinsic Spatial Resolution. Starting from the CFOV of the PET subsystem, the point source was attached to a translation stage and stepped at 0.4 mm steps across 13 crystals along the long axis of the FOV (half axial length of a detector module). Due to geometric restriction by the side detectors, the point source could not be stepped across half of the detector module along the short axis. Instead, the source was stepped across the central fourteen crystals in a transverse plane of a detector module. Acquisition time was 60 seconds at each location. Coincidence counts for directly opposing crystal pairs were plotted as a function of source location. The count distribution of each crystal pair was fitted with a Gaussian function and the FWHM determined the intrinsic spatial resolution of the detectors.

Image Spatial Resolution. The point source was imaged at two axial locations: (a) the center of the axial FOV and (b) one fourth of the axial FOV, 23.8 mm from the center along the axial direction. For each of these locations, the source was placed at 0 mm, 5 mm, 10 mm and 15 mm from the geometric center along the transverse FOV. Acquisition time was 1 minute at each position and more than 10^5 prompt counts were acquired per measurement. The NEMA NU-4 document also recommends measurements at 20 mm and 25

mm from the center, which are not included in this study due to the geometric restriction. Due to the box shaped geometry of the tomograph, conventional filtered backprojection reconstruction is not available and therefore in a significant deviation of the NEMA protocol, images were reconstructed using the MLEM algorithm. As specified in the NEMA NU-4 2008 protocol, the response function was formed by summing one-dimensional profiles that were parallel to the radial, tangential, and axial directions. A parabolic fit of the peak point and its two nearest neighboring points was used to determine the maximum value of the response function. Linear interpolation between adjacent pixels was used to determine the position of the half and one tenth of the parabolic curve maximum.

Sensitivity

A ^{68}Ge point-like source (Eckert & Ziegler Isotope Products, Valencia, CA) embedded in thin steel tubing was used to measure absolute sensitivity. The thin steel casing ensures annihilation of all the positrons, with only nominal attenuation of the 511 keV gamma rays, which was assumed to be insignificant in this study. The activity of the point source was 1.62 kBq measured in a calibrated well-type gamma counter (Wallac Wizard 1480, Perkin Elmer, Shelton, CT). The activity was low enough so that the counting losses were less than one percent and the randoms rate less than 5% of the true event rate, fulfilling the NEMA NU 4-2008 recommendations. The axial sensitivity profile was measured with the ^{68}Ge source stepped from end to end of the axial FOV, with the axial positions of the source determined from the reconstructed images. The number of coincidences was recorded at each position for 60 seconds. Delayed coincidences were subtracted from prompts before the true coincidences were divided by the actual source activity. This ratio was corrected for the branching ratio of ^{68}Ga (0.89), but the attenuation of the steel material surrounding the source was not compensated. The average sensitivity for a mouse-sized object (with a 7 cm axial length) was calculated from the measured axial sensitivity profile.

Scatter and Count-Rate Performance

Count-rate performance was evaluated using the NEMA NU-4 mouse-sized phantom, which is a 70 mm long and 25mm diameter solid cylinder made of high density polyethylene (0.96 g/cm3), with a 3.2 mm diameter hole drilled parallel to the central axis at a radial offset of 10 mm. A flexible tube filled with

^{18}F solution was inserted into the 3.2 mm hole of the phantom. The initial activity was measured to be 18.8 MBq using a dose calibrator (Atomlab 300; Biodex Medical Systems, Upton, NY) at the start of the acquisition. The phantom was centered in the FOV and rotated by 45 degrees to achieve a more symmetric source distribution that is also a closer representation of the expected spatial distribution in mouse studies. A life supporting chamber was included in the FOV for this measurement, creating a more realistic scatter environment.

The data was processed as specified by NEMA NU-4. The scatter fraction was measured using a prompt sinogram with an activity of 185 kBq. This low activity frame was chosen to ensure that dead time and randoms did not affect the measurement. The scattered count rate was then calculated by Equation 1:

$$R_{scatter} = R_{prompt} - R_{true} - R_{random}, \qquad (1)$$

where $R_{scatter}$, R_{prompt}, R_{true} and R_{random} are the scatter, prompt, true and random event rates, respectively. The scatter fraction (SF) was calculated by Equation 2:

$$SF = \frac{R_{scatter}}{R_{scatter} + R_{true}}, \qquad (2)$$

The noise equivalent count rate (NECR) for each prompt sinogram was determined using the following equation:

$$NECR = \frac{R_{true}^2}{R_{prompt} + R_{random}} = \frac{(R_{prompt} - R_{random})^2 \times (1 - SF)^2}{R_{prompt} + R_{random}} \qquad (3)$$

CT Subsystem Performance

For the x-ray CT subsystem, noise, dose, contrast and spatial resolution were measured. First, a 25-mm diameter plastic cylinder filled with water was imaged, and noise was calculated as the ratio of the standard deviation over the average value in a 4000 mm^3 uniform region. Dose was measured by placing a 10-cm long, pencil-shaped ionization chamber, model 10X5-3CT (Radcal Corporation, Monrovia, CA) in a life supporting chamber (including the cover) and acquiring a scan with the standard protocol. The 10

cm wire was entirely in the x-ray cone beam (10.6 cm). The dose was measured five times and averaged. For image contrast, a 25-mm diameter lucite phantom containing six 2-mm diameter rods containing four iodine concentrations (750, 250, 50 and 0 mg/cc) was scanned. The average image value in each rod was calculated and plotted against the nominal rod iodine concentration. Linearity was assessed by the coefficient of determination (R^2) of a linear regression (ordinary least squares). Finally, resolution was measured with a micro-CT wire phantom (QRM GmbH, Moehrendorf, Germany) containing a 25-µm diameter Tungsten wire. The Fourier Transform of a profile across the image (line-spread function) was used to calculate the modulation transfer function (MTF) and we report the resolution as the value of the MTF at 10% of the maximum.

Imaging Studies

NEMA Phantom Study. Image quality studies were performed using the NEMA NU-4 image quality phantom. The phantom (Data Spectrum Corporation, Hillsborough, NC) consists of three regions: a main fillable uniform region allowing the uniformity to be measured; a lid that attaches to the main fillable region, containing 2 smaller cold regions (filled with water and air) used to quantify the spillover ratio (SOR); and a solid acrylic region with 5 cylindrical holes for measuring the recovery coefficients as a function of rod diameter. Since the G8 was designed for use with a low injection dose, the image-quality phantom was filled with 1.85 MBq ^{18}F solution measured with a dose calibrator (Atomlab 300; Biodex Medical Systems). It should be pointed out that this activity is half the activity level recommended by the NEMA NU-4 protocol. The phantom was placed on a life supporting chamber to simulate *in vivo* imaging and data was acquired for 20 minutes as prescribed in the NEMA NU-4 protocol. Detector efficiency normalization and random event corrections were applied, but no scatter correction was applied. A CT scan of the phantom and its supporting bed was acquired and the reconstructed CT image defining the data acquisition geometry was forward projected through the PET system response matrix to generate attenuation correction of the PET data.

A 22.5-mm-diameter and 10-mm-high cylindrical volume of interest (VOI) was drawn over the center of the uniform region of the image-quality phantom. The average concentration values and standard deviation (SD) in this VOI were measured to estimate the noise performance as a measure of uniformity. The image slices covering the central 10-mm length of the rods were averaged to obtain a single image slice of lower noise. Circular regions of interest (ROIs) were drawn in this image around each rod, with diameters twice the physical diameters of the rods. The maximum values in each of these ROIs were measured and divided by the mean value obtained in the uniformity test to obtain the recovery coefficient (RC) for each rod size. The transverse image pixel coordinates of the locations with the maximum ROI values were recorded and used to create 10 mm long line profiles along the rods in the axial direction. The SD of the pixel values measured along each of these line profiles was calculated. Although no scatter correction was applied to the acquired dataset, the SOR of the water- and air-filled cold region chamber were calculated as specified in the NEMA NU-4 standard to provide a rough estimation of the scatter effects. The diameter of the VOI was 4 mm and encompassed the central 7.5 mm in length in the axial direction. The ratio of the mean in each cold region to the mean of the hot uniform area was reported as SOR.

Mouse Study. The UCLA Animal Research Committee approved the animal studies which were carried out according to the guidelines of the Department of Laboratory Animal Medicine at UCLA. C57BL6 mice were anesthetized with 2% isoflurane in oxygen and injected intravenously via tail vein with 2.78 MBq 18F-FDG or 2.70 MBq 89Zr-anti-CD8 antibody. Animals were kept warm on heating pads throughput the imaging procedures. After 60 min (18F-FDG) or 6 days (89Zr-anti-CD8 antibody) of tracer biodistribution, mice were anesthetized and placed in dedicated G8 imaging chambers for PET/CT imaging. PET scans were acquired for 10 min (18F-FDG) or 20 min (89Zr-anti-CD8) with an energy window of 350-650 keV reconstructed using ML-EM, followed by CT acquisition. All PET images were corrected for CT-based photon attenuation, detector normalization and radioisotope decay (scatter correction was not applied) and converted to units of percent injected dose per gram (%ID/g). Images were analyzed using AMIDE v1.0.4 (*23*) and OsiriX (http://www.osirix-viewer.com).

RESULTS

Energy Resolution and Flood Histograms

Supplemental Figures 1A and B show the flood images acquired from two detector modules in one panel. For the crystals in all four panels, the measured energy resolution ranged from 15.0 % to 69.6 % FWHM, with a mean of 19.3±3.7 %. Supplemental Figure 1C shows a vertical profile across one column of crystals shown in Supplemental Figure 1A with a peak to valley ratio (PVR) of 4.5, and Supplemental Figure 1D shows a horizontal profile across one row of crystals shown in Supplemental Figure 1B with a PVR of 4.8.

Spatial Resolution

Intrinsic Spatial Resolution. The intrinsic spatial resolution of an opposing detector pair is shown in Figure 2. For crystal pairs along the detector short axis, the measured FWHM ranges from 1.16 mm to 1.41 mm, with an average value of 1.30±0.08 mm. For crystal pairs along the detector long axis, the measured FWHM ranges from 1.27 mm to 1.64 mm, with an average value of 1.38±0.10 mm.

Image Spatial Resolution. Figures 3A and B show the reconstructed image spatial resolution in the radial, tangential, and axial directions measured in the central and 1/4 axial transverse plane, ranging from 0.60 mm to 1.01 mm, with an average value of 0.81±0.11 mm.

Sensitivity

Table 2 summarizes the absolute system sensitivity for different energy window settings at 10 mm from the axial center towards the axial edge of the FOV, as well as for the axial center of the FOV. The maximum system sensitivity is 17.8% measured at 10 mm from the axial CFOV and with an LLD of 150 keV.

In previous work an LLD of 350 keV was recommended as the optimized energy threshold for PET systems with detector geometries such as the G8 (*17*). With the optimal energy window of 350–650 keV, the G8 has a peak system sensitivity of 9.0% measured at 10 mm from the axial CFOV. At the axial CFOV, the sensitivity is 8.6%. The axial sensitivity profile with the energy window of 350-650 keV is shown in Figure 4. The average sensitivity for a mouse-sized object (7 cm axial length) is 6.8%.

Scatter and Count-Rate Performance

The prompt, random and NEC rates as a function of total activity in the mouse-sized phantom are plotted in Figure 5. The prompt rates reach peak values at around 3.6 MBq total activity. With this activity, the random events account for approximately 7% of the total prompt counts. The peak NECR is 44 kcps achieved at a total phantom activity of 2.9 MBq . The scatter fraction for the mouse-sized phantom is 11%.

CT Subsystem Performance

The calculated noise level in the uniform region of the water cylinder is 2.8%. The average dose per scan is measured as 50.1±1.2 mGy. The G8 CT does not have a mechanical shutter in front of the x-ray source and therefore, while the system is waiting for the source voltage to ramp-up and the current to stabilize, some dose is given to the subject. This contribution was estimated to be about 7 mGy or 14% of the total dose received. The contrast linearity (the CT value in the reconstructed image against iodine concentration for each rod) is excellent both visually and as expressed by the coefficient of determination $R^2 = 0.9998$. The MTF (10%) of the CT system was 2.05 cycles/mm. This approximately corresponds to a FWHM of 0.4 mm.

Imaging Studies

NEMA Phantom Study. Figure 6 shows the images (single slice, 0.46 mm thick) of a transverse plane of the uniform region (A), a coronal plane (B), a transverse plane with the five resolution recovery rods (C), and a profile across the uniform area (D) of the NEMA image quality phantom. With the ML-EM reconstruction, the SD in the uniform region was 7.7%. The RCs for the five different rod sizes from 1 to 5 mm diameter are 0.11±0.01, 0.70±0.08, 1.07±0.09, 1.10±0.11 and 1.04±0.09. The SORs measured in the water and air filled cold region chambers are 7.5±2.1% and 5.4±1.2%.

Mouse Study. Representative images of the biodistribution of two PET tracers radiolabeled with different radioisotopes, ^{18}F-FDG and ^{89}Zr-anti-CD8 antibody, are shown in Figure 7. Figure 7A shows coronal and sagittal images from a 10-min ^{18}F-FDG study in C57BL6 mice, distinguishing the myocardium from blood pool and identifying other tissues such as Harderian glands, brain including cerebellum, spinal column, intestines, kidneys and bladder. The activity in the entire mouse was 1.96 MBq at scan time. Figure 7B illustrates the capabilities of the PET/CT combination system in a study of immunocompetent C57BL6

mice injected with ^{89}Zr-anti-CD8 antibody. A reconstructed three-dimensional volumetric PET image was registered with the CT dataset. The maximum intensity projection image of a 20 min scan shows well-defined mappings of the lymphoid organs of spleen, thymus, and lymph nodes, particularly axillary, brachial, cervical, inguinal, and popliteal lymph nodes. Expected biodistribution to liver, kidneys and bone were also observed. The activity in the entire mouse was 0.34 MBq at scan time.

DISCUSSION

This investigation has evaluated the overall performance of the G8 PET/CT preclinical system. The PET component was evaluated according to the NEMA NU-4 standards with modifications as necessary. Noise, dose level, contrast and resolution were evaluated for the CT component.

Besides an addition of two extra rows of crystals at the transverse edges of the FOV which reduces the gap between detectors, slightly different crystal dimensions and segmented lightguides, a major change from the G4 to the G8 system is the data acquisition electronics used for detector signal digitization and processing. The G8 employs upgraded data acquisition electronics with twice the number of ADC channels. The outputs from each of the MAPMTs in one detector panel are separately multiplexed into four signals (energy, X, Y and dynode), and eight ADCs are used to process the signals from each detector panel.

The increased granularity of the detector readout scheme in the G8 leads to an extended system dynamic range and better count rate performance. In the G4, the NECR peak was reached at lower total activity than for comparable instruments, due to its compact system geometry, the long decay time of BGO and the multiplexed electronics (*12,15*). For each gamma interaction in a detector module, the BGO signal is integrated for 800 ns, during which no new event detection is possible. In the G8, when a gamma photon interacts with one of the two modules in one detector panel, the other module is still capable for event detection since the two modules in one panel are optically isolated and readout separately. As a result, the activity at the NECR curve peak for the G8 is nearly double at 2.9 MBq, compared with 1.5 MBq for the G4. The design goal of the G8 has been high sensitivity imaging of mice at low injected dose, so imaging with the dose higher than the NECR peak activity is not recommended. The detector would be saturated with pulse pileup, which may introduce image artifacts and compromise the spatial resolution performance.

The system though can be used with much lower amounts of injected activity than is typical in the field (e.g. 0.34 MBq ^{89}Zr shown in Figure 7).

The new readout scheme also includes modifications on the detector and lightguide design. For each detector panel in the G4, one BGO scintillator array is coupled to two MAPMTs via a 1 mm clear glass. The scintillation light from crystals at the junction of the two MAPMTs is distributed to both MAPMTs. Light collection for these crystals is diminished because of the large insensitive area at the junction, degrading crystal identification and energy resolution. In the G8, each detector panel consists of two separate and optically isolated BGO scintillator arrays. Each array is coupled to the sensitive area of one MAPMT using a tapered, pixelated lightguide. As a result, the loss of light at the PMT junction area is reduced (*24*).

The sensitivity measured at the CFOV is lower than that at ±10 mm axial offsets as shown in Figure 4, which also results from the new detector readout scheme used in the G8. When an annihilation gamma interacts via scattering in two crystal arrays within one detector panel, the energy deposited in each crystal array will be detected as a separate event. This increases the probability that neither of the two detections is qualified in the energy window of 350-650 keV. As a result, a fraction of the events happening at the edge crystal between the two detectors in one panel will be rejected, reducing the measured sensitivity at the CFOV. This loss of events could also be observed in the intrinsic spatial resolution result. The number of counts for the left two profiles in Figure 2B, which correspond to the edge crystals close to the junction of two crystal arrays, are lower than that for other profiles. The use of measured sensitivity at the CFOV (8.6%) as the system peak sensitivity significantly underestimates the G8 system performance. The sensitivity for mouse imaging (6.8%) averaged from the 7 cm axial length of the sensitivity profile is a more suitable parameter and compares favorably with other systems (*25*). For the measured sensitivity reported in this work, the attenuation of the steel material surrounding the source was not compensated.

The MLEM reconstructed image spatial resolution shown in Figure 3 is fairly homogeneous within the entire FOV. It is because the flat panel box like geometry of the G8 leads to DOI errors that are more uniformly distributed in the FOV. It also demonstrates the MLEM reconstruction implemented accurately

models the physical response of the scanner in the system matrix, despite the fact that the detection of coincidences along very oblique angles are allowed owing to the close geometry of the scanner. The image spatial resolution averages at 0.8 mm FWHM, which is consistent with the choice of the reconstructed image voxel size ($0.46 \times 0.46 \times 0.46$ mm^3), showing the reconstruction is implemented properly. However, this value is not representative of the actual image spatial resolution of the system during *in vivo* imaging, since the method of measuring the image spatial resolution defined in the NEMA NU4-2008 standard is incompatible with the iterative reconstruction algorithm. As the G8 system does not provide traditional filtered back projection image reconstruction, we report here the iterative image reconstruction results as a reference. For *in vivo* studies, the crystal size and the detector intrinsic spatial resolution (~1.4 mm) are better indicators for the reconstructed image spatial resolution.

CONCLUSION

This study evaluated the performance of the G8 integrated PET/CT system. With an energy window of 350–650 keV, the peak absolute sensitivity is measured 9.0% near the CFOV, and the average sensitivity for imaging a mouse-sized object (7 cm axial length) is 6.8%. The total activity at the peak NECR for the mouse-sized phantom is 2.9 MBq (78 μCi). The dynamic range of the G8 is significantly improved with respect to the previous generation G4. The overall performance demonstrates that the G8 scanner is suitable for producing high quality images for molecular imaging based biomedical research.

ACKNOWLEDGEMENTS

The authors would like to thank Richard Tavaré and Kirstin Zettlitz from the Anna Wu Lab at the Crump Institute for Molecular Imaging at UCLA for providing the Zr89-anti-CD8 antibody, and the staff of the UCLA Ahmanson Biomedical Cyclotron Facility for providing ^{18}F-ion and ^{18}F-FDG. We would like to thank Waldemar Ladno and Olga Sergeeva of the Crump Institute's Preclinical Imaging Technology Center for their assistance with the imaging for this study.

DISCLOSURE

Nam T. Vu and Zheng Gu are currently employees of Sofie Biosciences, Inc. Nam T. Vu and Arion F. Chatziioannou are shareholders of Sofie Biosciences, Inc.

This work was supported by the UCLA Foundation from a donation made by Ralph and Marjorie Crump for the UCLA Crump Institute for Molecular Imaging and in part by the National Cancer Institute P30 CA016042 Cancer Center Support Grant.

No other potential conflicts of interest relevant to this article exist.

REFERENCES

1. Phelps ME. Positron emission tomography provides molecular imaging of biological processes. *Proc Natl Acad Sci U S A.* 2000;97:9226-9233.

2. Gambhir SS. Molecular imaging of cancer with positron emission tomography. *Nat Rev Cancer.* 2002;2:683-693.

3. Myers R. The biological application of small animal PET imaging. *Nucl Med Biol.* 2001;28:585-593.

4. Chatziioannou AF. Molecular imaging of small animals with dedicated PET tomographs. *Eur J Nucl Med.* 2002;29:98-114.

5. Townsend DW. Dual-modality imaging: Combining anatomy and function. *J Nucl Med.* 2008;49:938-955.

6. von Schulthess GK, Schlemmer HPW. A look ahead: PET/MR versus PET/CT. *Eur J Nucl Med Mol Imaging.* 2009;36:3-9.

7. Clark DP, Badea CT. Micro-CT of rodents: State-of-the-art and future perspectives. *Physica Medica-European Journal of Medical Physics.* 2014;30:619-634.

8. Kinahan PE, Townsend DW, Beyer T, Sashin D. Attenuation correction for a combined 3D PET/CT scanner. *Med Phys.* 1998;25:2046-2053.

9. Watson CC, Casey ME, Michel C, Bendriem B. Advances in scatter correction for 3D PET/CT. *IEEE Nucl Sci Symp Conf Rec.* 2004;1-7:3008-3012.

10. Erlandsson K, Buvat I, Pretorius PH, Thomas BA, Hutton BF. A review of partial volume correction techniques for emission tomography and their applications in neurology, cardiology and oncology. *Phys Med Biol.* 2012;57:R119-R159.

11. Wang HK, Stout DB, Chatziioannou AF. Estimation of mouse organ locations through registration of a statistical mouse atlas with Micro-CT images. *IEEE Trans Med Imaging.* 2012;31:88-102.

12. Gu Z, Taschereau R, Vu NT, et al. NEMA NU-4 performance evaluation of PETbox4, a high sensitivity dedicated PET preclinical tomograph. *Phys Med Biol.* 2013;58:3791-3814.

13. Herrmann K, Dahlbom M, Nathanson D, et al. Evaluation of the Genisys4, a bench-top preclinical PET scanner. *J Nucl Med.* 2013;54:1162-1167.

14. National Electrical Manufacturers Association (NEMA). Performance measurements of small animal positron emission tomographs. *NEMA Standards Publication NU 4-2008*. Rosslyn, VA: NEMA; 2008:23.

15. Gu Z, Prout DL, Taschereau R, Bai B, Chatziioannou AF. A new pulse pileup rejection method based on position shift identification. *IEEE Trans Nucl Sci.* 2016;63:22-29.

16. Douraghy A, Rannou FR, Silverman RW, Chatziioannou AF. FPGA electronics for OPET: A dual-modality optical and positron emission tomograph. *IEEE Trans Nucl Sci.* 2008;55:2541-2545.

17. Gu Z, Bao Q, Taschereau R, Wang H, Bai B, Chatziioannou AF. Optimization of the energy window for PETbox4, a preclinical PET tomograph with a small inner diameter. *IEEE Trans Nucl Sci.* 2014;61:1164-1173.

18. Mumcuoglu EU, Leahy R, Cherry SR, Zhou ZY. Fast gradient-based methods for Bayesian reconstruction of transmission and emission PET images. *IEEE Trans Med Imaging.* 1994;13:687-701.

19. Taschereau R, Rannou FR, Chatziioannou AF. A modeled point spread function for a noise-free system matrix. *IEEE Nucl Sci Symp Conf Rec.* 2011:4102-4105.

20. Feldkamp LA, Davis LC, Kress JW. Practical cone-beam algorithm. *J Opt Soc Am A Opt Image Sci Vis.* 1984;1:612-619.

21. Suckow C, Kuntner C, Chow P, Silverman R, Chatziioannou A, Stout D. Multimodality rodent imaging chambers for use under barrier conditions with gas anesthesia. *Mol Imaging Biol.* 2009;11:100-106.

22. Chow PL, Stout DB, Komisopoulou E, Chatziioannou AF. A method of image registration for small animal, multi-modality imaging. *Phys Med Biol.* 2006;51:379-390.

23. Loening AM, Gambhir SS. AMIDE: a free software tool for multimodality medical image analysis. *Mol Imaging.* 2003;2:131-137.

24. Gu Z, Prout DL, Valenciaga Y, Chatziioannou AF. Lightguides for improving edge crystal identification and energy resolution in pixelated scintillator detectors. *IEEE Nucl Sci Symp Conf Rec.* 2015.

25. Goertzen AL, Bao QN, Bergeron M, et al. NEMA NU 4-2008 comparison of preclinical PET imaging systems. *J Nucl Med.* 2012;53:1300-1309.

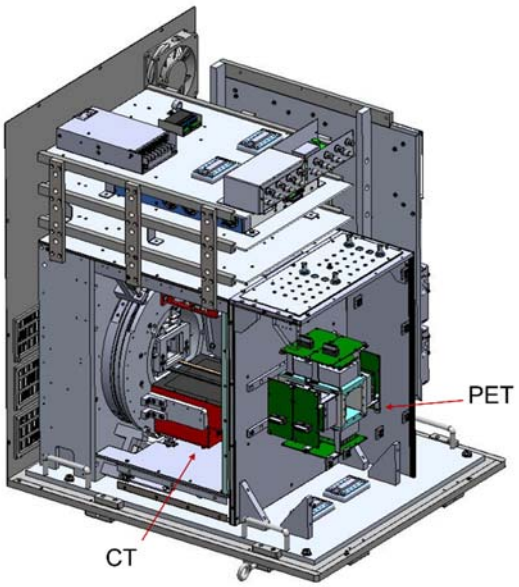

FIGURE 1. Schematic of the G8 PET/CT tomograph.

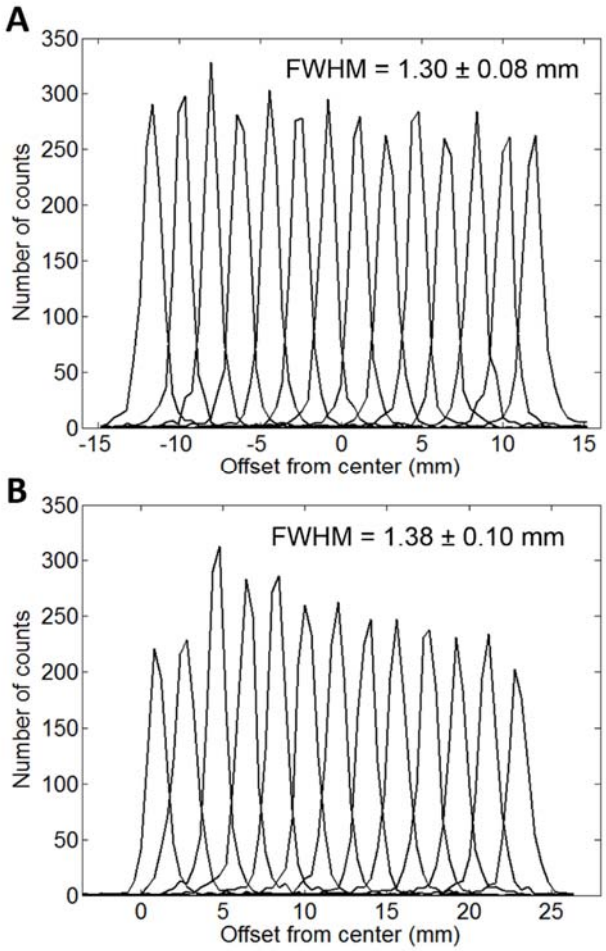

FIGURE 2. Intrinsic spatial resolution measured with a ^{22}Na point source in the direction (A) along the detector short axis and (B) along the detector long axis.

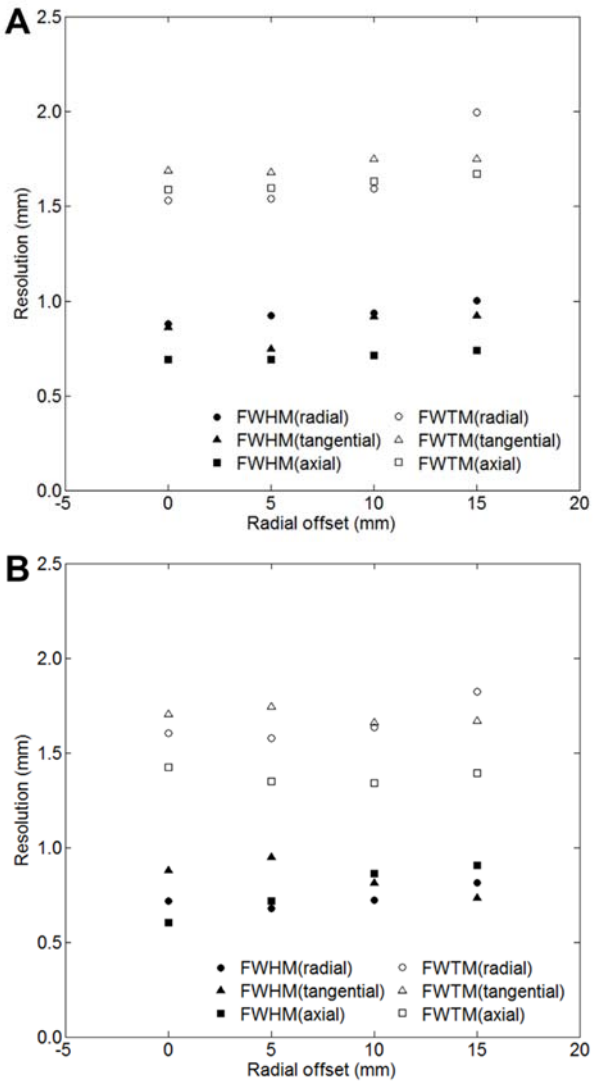

FIGURE 3. MLEM reconstructed image spatial resolution of the G8 system, showing the FWHM and FWTM of the radial, tangential, and axial image resolution at (A) axial center of the FOV and (B) 23.75 mm from the axial center towards the axial edge of the FOV.

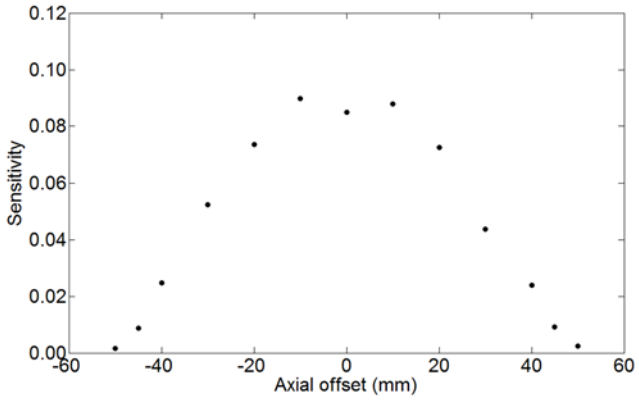

FIGURE 4. Absolute system sensitivity as a function of axial position. The energy window was 350-650 keV.

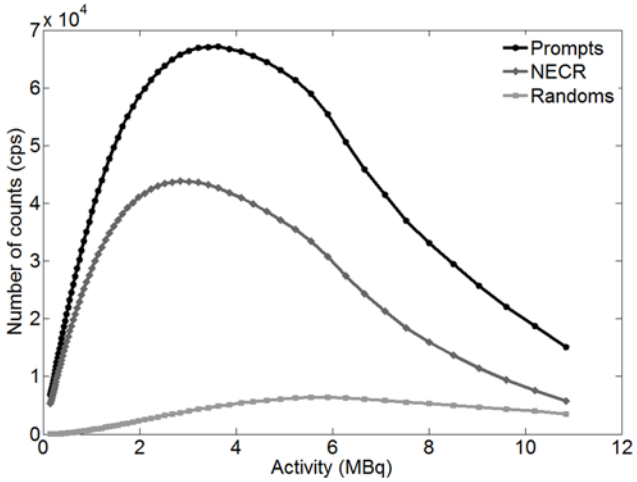

FIGURE 5. Count rate of the G8 system as a function of line source activity.

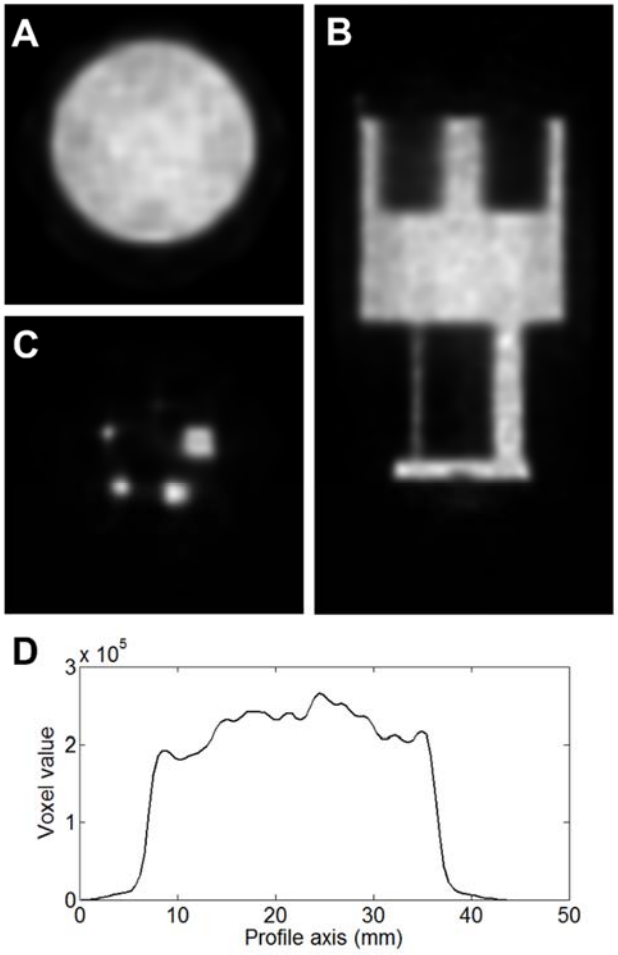

FIGURE 6. Reconstructed Images of the NEMA NU-4 image quality phantom, filled with ^{18}F (1.85 MBq) and imaged for 20 minutes: (A) transverse slice of the uniform region; (B) coronal slice; (C) transverse slice of the rods region; (D) profile across the uniform area.

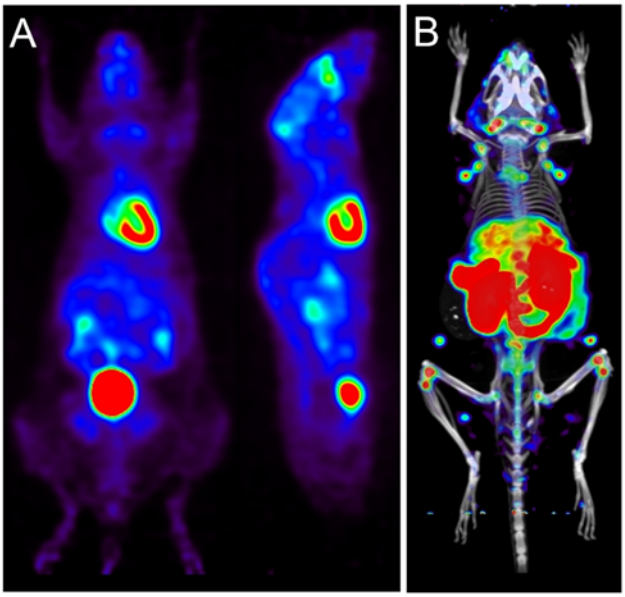

FIGURE 7. Reconstructed images of C57BL6 mice injected with ^{18}F-FDG and ^{89}Zr-anti-CD8 antibody: (A) 10-min static PET coronal and sagittal slices of a mouse 60 min after injection of ^{18}F-FDG (1.96 MBq at scan time); (B) 20-min static PET/CT maximum intensity projection of a mouse 6 days after injection of ^{89}Zr-anti-CD8 antibody (0.34 MBq at scan time).

TABLE 1

Characteristics of the G4 and the G8 systems

	G4	G8
Crystal material	BGO	BGO
Crystal size	1.75 x 1.75 x 7.2 mm^3	1.75 x 1.75 x 7.2 mm^3
Crystal pitch	1.83 mm	1.83 mm
Crystal array	24 x 26 crystals/PMT	26 x 26 crystals/PMT
Light guide	1 mm thick glass layer	Tapered, pixelated light guide
PMT	Hamamatsu H8500 MAPMT	Hamamatsu H8500 MAPMT
Number of detector modules	4	8
Number of crystals per module	1248	676
Number of crystals in total	4992	5408
Number of ADCs	16	32
Signal processing system	VHS-ADC (Lyrtech, Quebec)	PicoDigitizer (Nutaq, Quebec)
Anatomical reference approach	X-ray projection and optical photographic images	CT

TABLE 2

Absolute System Sensitivity (%) as a Function of LLD at 10 mm from the Axial Center towards the Axial Edge of the FOV, and at the Axial Center of the FOV

LLD (keV)	150	200	250	300	350
10 mm axial offset	17.8	14.8	11.9	10.1	9.0
CFOV	16.8	14.0	11.4	9.7	8.6

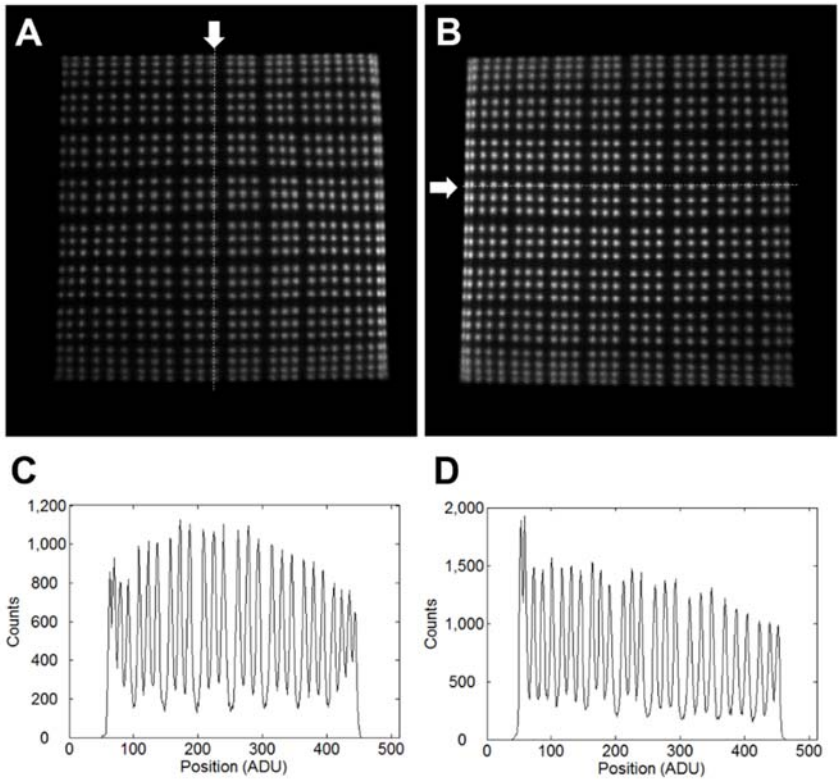

SUPPLEMENTAL FIGURE 1. (A) and (B): flood images acquired from two detector modules in one of the four detector panels; (C) a vertical profile across one column of crystals; (D) a horizontal profile across one row of crystals.